ADVANCED FUNCTIONAL MATERIALS
www.afm-journal.de

Rapid Closed Pore Regulation of Biomass-derived Hard Carbons Based on Flash Joule Heating for Enhanced Sodium Ion Storage

Yuqian Qiu, Yanxia Su, Xiaohan Jing, Hao Xiong, Duo Weng, Jian-Gan Wang, Fei Xu, and Hongqiang Wang**

Closed pores are essential for enhancing the low-potential (<0.1 V) plateau capacity and initial Coulombic efficiency of hard carbon (HC) anode materials for energy-dense sodium-ion batteries. However, the lack of simple and effective closed-pore construction strategies has severely hindered their future commercialization. Herein, a rapid closed-pore regulation strategy for biomass-derived HCs is proposed through pre-heat treatment followed by flash Joule heating (FJH). The pre-heat treatment is critical for transforming vulnerable biomass into high-carbonizability frameworks that are resistant to over-graphitization. FJH treatment helps to generate enriched closed pores surrounded by the resulting carbon walls with expanded interlayer spacing as accessible Na^+ channels. This strategy shows remarkable universality and applicability for biomass feedstocks, enabling rapid conversion of various carbonization-vulnerable precursors to high-yield (e.g. HC600-J-1500 compared with HC25-J-1500, ≈14-fold yield increase) and closed-pore enriched HCs. The optimized sample demonstrates an outstanding reversible capacity of 377 mAh g^{-1} with a superior initial Coulombic efficiency of 93.3%, which stands in a record value prepared with FJH and is even competitive via conventional carbonization. Comprehensive tests reveal that the efficient Na storage originates from the pore-filling mechanism in the closed nanopores. This work suggests a facile and universal closed-pore regulation approach for the rational design of high-performance HCs.

1. Introduction

Hard carbons (HCs) have attracted considerable attention as the most close-to-commerce anode materials for sodium-ion batteries (SIBs), due to their distinctive structural characteristics, including tunable interlayer spacing and abundant voids to accommodate Na^+.[1] However, this complex structure also poses challenges, as the sodium storage mechanism remains controversial.[2] Fortunately, it has been recognized that low-potential plateau capacity is the dominant source of overall sodium storage capacity and plays an essential role in determining the output voltage and the energy density of the full cells.[3] Therefore, much effort has been devoted to developing plateau-dominated, high-capacity HCs,[4] highly associated with graphitic and pore microstructures. The state-of-the-art investigation has reached a consensus that appropriately sized closed nanopores with Na cluster filling can significantly prolong low-potential plateau capacity.[5] Meanwhile, such an enhanced capacity triggered by closed pore-filling does not show diminished initial Coulombic efficiency (ICE) owing to a tiny increase in the contact area between electrolyte and electrode with internal close pores. Consequently, the design and construction of closed pores are becoming thriving and rewarding in the field of HCs.

Various closed pore-forming strategies have been established, such as controlling the carbonization process,[6] tightening the pore entrances of porous carbons,[7] templating with pore-forming agents/components,[8] and chemical activation,[9] etc. These works partialy explored the mechanism of closed pore formation and enabled delicate regulation of closed pores in HCs.[10] However, these approaches involve complex and time-consuming procedures such as template removal,[8] chemical activation,[11] or chemical vapor deposition processes.[7] Besides, these approaches are usually based on furnace heating treatment for carbonization, which generally takes dozens of hours with heating/holding/cooling and is thus energy consumptive. Thus, it is necessary to seek a rapid and facile strategy to synthesize HCs with enriched closed pores.

Flash Joule heating (FJH), known for its rapid high-temperature treatment with high efficiency and low cost,[12] has been well explored in fabricating energy storage materials such

Y. Qiu, Y. Su, X. Jing, H. Xiong, D. Weng, J.-G. Wang, F. Xu, H. Wang
State Key Laboratory of Solidification Processing
Center for Nano Energy Materials
School of Materials Science and Engineering
Northwestern Polytechnical University and Shaanxi Joint Laboratory of Graphene (NPU)
Xi'an 710072, P. R. China
E-mail: feixu@nwpu.edu.cn; Hongqiang.Wang@nwpu.edu.cn
D. Weng
Shaanxi Coal Chemical Industry Technology Research Institute Co., Ltd
Xi'an 710100, P. R. China
The ORCID identification number(s) for the author(s) of this article can be found under https://doi.org/10.1002/adfm.202423559

DOI: 10.1002/adfm.202423559

as ceramics,[13] alloys,[14] and carbon materials,[15] with its scalability attracting increasing attention.[16] Current applications of FJH include ceramics for solid-state batteries,[17] high-entropy alloy catalysts for lithium-sulfur batteries,[18] and carbon-based materials such as graphene for lithium-ion batteries.[19] Despite the progress in these areas, the use of FJH in designing HCs for SIBs remains relatively underexplored, with only serveral articles addressing this topic rencently.[4c,20] It has been demonstrated that the defective structure, graphitic micro-domains, and closed pores in HCs can be effectively regulated via FJH, through strategies such as increasing the pressure during the FJH process,[20b–d] enhancing the frequency of FJH process,[20d] or changing pulses of different widths[4c] thereby significantly enhancing Na storage performance. However, these works are mainly based on carbon microstructure reconstruction via post-treatment of commercial HCs[4c,20c] or carbons by pre-pyrolysis even to 800 °C.[4c,20d] The use of pre-prepared carbons rather than organic precursors could significantly limit the structural diversity and flexibility in manipulating the resulting HC microstructures, and thus the majority of reported works showcase a limited capacity of less than 310 mAh g^{-1} and ICE no more than 90%.[20a,b,d] However, the utilization of organic precursors with FJH to design high-performance HCs remains a great challenge. This is because in comparison to traditional furnace heating methods, FJH featured by blackbody radiation via an external electric field, can release most of the heat within milliseconds, leading to rapid heating and fast cooling processes.[15] Consequently, tremendous gaseous small molecules were generated and immediately carried away by the flowing protective gas, leaving behind a few times for radical coupling, molecular rearrangement, condensation, aromatization, and solidification, thus giving rise to diminished carbonization yield or even completely burned off. Only those precursors containing easy graphitizable components would survive the extreme heating/cooling conditions of FJH, thus forming highly graphitic structures with reduced interlayer spacing and low closed porosity unfavorable for efficient Na ion storage.[10,21] Otherwise, a highly defective structure was generated with FJH under moderate carbonization temperature (<1300 °C),[20a,c] as also revealed by the conventional furnace heating that a fast heating rate facilitates more defective structures.[22] Therefore, HCs generated at moderate carbonization temperatures with the rapid FJH process show quite low ICE, which is <60%.[20a,d] These results suggest that there are more rigorous requirements for organic precursors, requiring robust frameworks to allow high carbonizability under the extreme heating rate of FJH. Therefore, it would be highly desirable to extend the concept of FJH with diverse precursors to enable elegant mediation of the microstructure, especially closed pores, for further enhanced performances.

Herein, we present an effective strategy by pre-heat treatment and further FJH that can get biomass-derived HCs with abundant closed pores and larger interlayer spacing for Na^+ access. By precisely controlling the pre-heat treatment temperature, we can accurately regulate open pore structure and get a high-carbonizability framework that is resistant to over-graphitization. Upon the subsequent FJH, enriched closed pores are rapidly created from the ultramicropores surrounded by the walls derived from the high-carbonizability framework (**Figure 1a**). This pre-heat treatment process leads to an increase in interlayer spacing, allowing for more accessible Na^+ channels within the material. We elucidate the structural evolution of carbon phases and closed nanopores under varying pre-heat treatment conditions and FJH processes to get a carbonization model of cellulose-derived HCs. Thus, the optimized sample achieves an ultrahigh reversible specific capacity of 377 mAh g^{-1}, and a superior ICE of 93.3% as the anode of SIBs. Comprehensive ex situ tests reveal that the high Na^+ storage performance originates from the pore-filling mechanism in the closed micropores. This study presents a facile and universal method for the formation of closed pores, facilitating the rational design of diverse biomass-derived HC pore structures.

2. Results and Discussion

2.1. The Influence Of Pre-Heat Treatment On Forming Closed Pores Of Hard Carbons

To evaluate the crystallinity of cellulose nanocrystals, X-ray diffraction (XRD) was conducted (Figure 1b), and the calculated crystallinity was 85.7%, comparatively higher than reported cellulose-based HC precursors.[23] Although high-crystallinity cellulose generally exhibited enhanced thermal stability due to its ordered structure,[24] the direct FJH process of HC25-J-1500 leads to only ≈1% carbonization yield (Figure 1c; Table S1, Supporting Information). Thermogravimetric analysis (TGA) was conducted to evaluate thermal stability, revealing cellulose nanocrystal residues of 38.5, 24.0, and 16.8 wt.% at 350, 400, and 600 °C, respectively (Figure 1d). Cellulose, a linear polysaccharide of *β*–*D*-glucose units linked by *β*-1,4-glycosidic bonds, lacks aromatic structures or conjugated systems, resulting in limited carbon skeleton stability.[25] It can be seen that the pyrolysis of cellulose typically follows three main stages.[23,26] At lower temperatures (<300 °C), cellulose undergoes dehydration, releasing water and some light volatile compounds. As the temperature increases to 300–400 °C, it reveals a primary decomposition peak, leading to the release of major pyrolysis products like *D*-glucopyranose and other volatiles.[27] The *D*-glucopyranose then participates in a series of polymerization, aromatization, and intramolecular condensation reactions that ultimately lead to the formation of biochar.[28] Complete inhibition of char formation (e.g., levoglucosenone) from cellulose occurred during fast pyrolysis in the presence of aromatic substances.[25b] In the final stage, the remaining solid undergoes further carbonization. This process yields a more durable, carbon-rich structure with higher thermal stability and increased graphitization. Therefore, preheat-treatment temperatures (350, 400, and 600 °C) were applied to cellulose-based HC samples (labeled as HC*xx*, where *xx* represents the preheat temperature), followed by FJH treatments (labeled as HC*xx*-J-*yy*, where *yy* represents the FJH temperature). Figure S1, (Supporting Information) demonstrates that the preheated HC600-J-1500 exhibited significantly higher weight, better uniformity, and darker coloration compared to that of HC25-J-1500. For instance, the yield of HC600-J-1500 achieved up to ≈14.1%. Accordingly, the total energy demand is calculated to be ≈45 kJ, and space-time-yield for the FJH process is calculated to be ≈1×10^6 kg m^{-3} h^{-1}, higher than the space-time-yield of coventional furnace heating, as shown the in the Supporting Information. Additionally, natural sources (coconut shells,

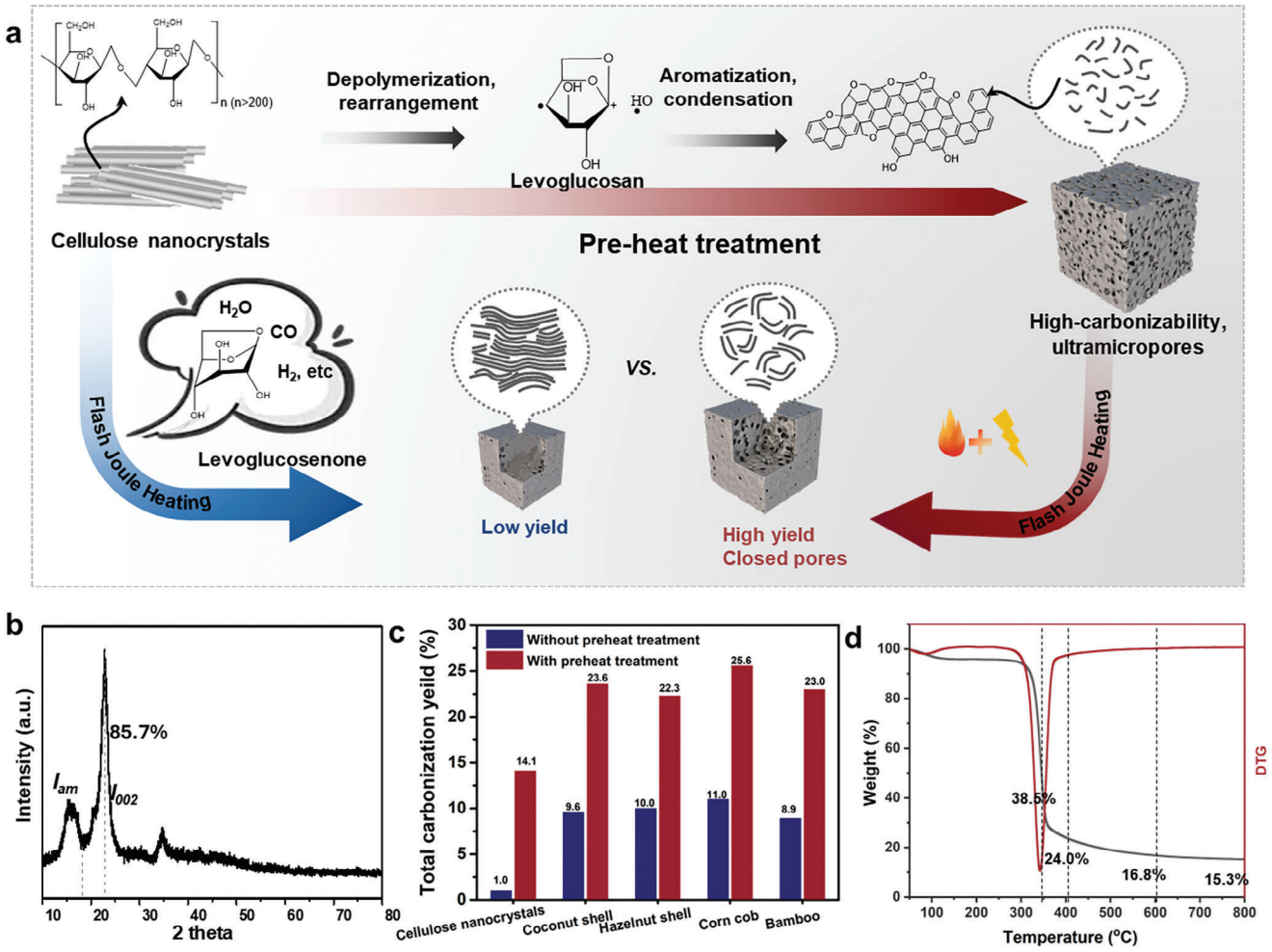

Figure 1. a) Schematic illustration of the process for fabricating HCs through pre-heat treatment and post-high-temperature FJH carbonization, whereas direct FJH carbonization without pre-heat treatment is presented for compare. b) The XRD pattern of cellulose nanocrystals. c) Total carbonization yield of different precursors. d) TGA and DTG curves of cellulose nanocrystals.

hazelnut shells, corn cobs, and bamboo) of HCs were utilized to evaluate the generalizability of this approach (Figure 1c; Figure S2 and Table S1, Supporting Information). Yields increase more than twice with preheat treatment, indicating a significant increase in efficiency. These natural biomass precursors exhibited significantly higher yields compared to cellulose nanocrystals, which may be attributed to their higher lignin content, structural complexity, and the presence of inorganic components such as potassium and calcium.[25,27b] Therefore, preheat treatment proved crucial for studying cellulose-based HC materials.

The micro-morphology of HCs was examined via transmission electron microscopy (TEM). Although all HCs showed a flake-like morphology at the micron scale (Figure S3, Supporting Information), distinct differences became evident at higher magnifications in high-resolution TEM (HR-TEM) images (**Figure** 2a,b) revealing significant structural differences between the samples. The microstructure of HC600-J-1500 exhibits a higher short-range order, typically formed by a combination of localized graphitized regions and amorphous carbon domains. Additionally, some pores are uniformly distributed within the walls derived from the high-carbonizability framework, reflecting localized structural rearrangements induced by high-temperature treatment. Due to the projection imaging mode of TEM, a completely accurate distinction between open and closed pores is not achievable. Morphological features indicative of closed pore structures are identified through HRTEM analysis and further corroborated by small-angle X-ray scattering (SAXS) and true density measurements in the next paragraph.[6a,29] Interlayer distances indicated an increase in HC600-J-1500, ranging from 0.351 to 0.417 nm, compared to HC25-J-1500 (0.343–0.385 nm). The larger interlayer spacing facilitates Na-ion transport and storage.[4a] The selected area electron diffraction (SAED) patterns showed attenuated diffraction rings in HC600-J-1500 as compared with that of HC25-J-1500, which indicates a lower degree of ordered structure in HC600-J-1500.[30]

The XRD patterns depicted in Figure 2c reveal two broad diffraction peaks ≈24° and ≈43° corresponding to (002) and (100) carbon planes across all samples subjected to varying preheat treatment temperatures. The sharp reflex observed in the XRD patterns corresponds to the (002) plane of graphitic carbon

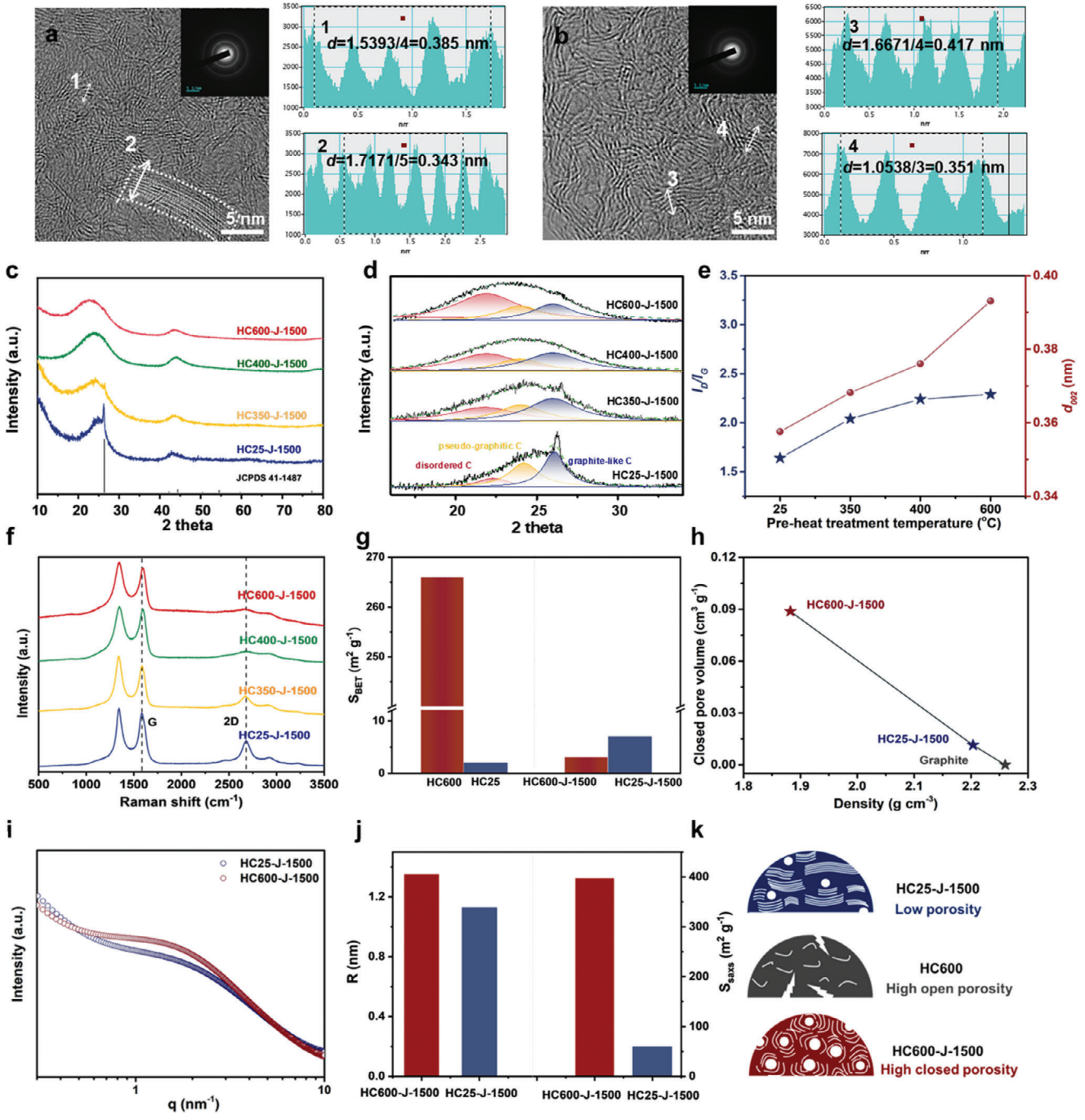

Figure 2. HRTEM and corresponding SAED images of a) HC25-J-1500 and b) HC600-J-1500. c) XRD patterns, d) XRD fitting curves, e) fitted value of d_{002} and $I_{D1}/I_{G,}$ and f) Raman curves of HC25-J-1500, HC350-J-1500, HC400-J-1500, and HC600-J-1500. g) S_{BET} of HC25, HC600, HC25-J-1500 and HC600-J-1500. h) The curve of true density and closed pore volume for HC25-J-1500 and HC600-J-1500. i) SAXS curves, j) fitting R and fitting S_{SAXS} of HC25-J-1500 and HC600-J-1500. k) Schematic illustration of the pore structure evolution during various thermal treatment processes.

in HC25-J-1500, indicative of regions with higher crystallinity formed. The deconvolution of XRD patterns in Figure 2d and the alignment with JCPDS 41–1487 of graphite in Figure 2c further support this assignment.[31] The sharp diffraction peaks in HC gradually disappear with increasing pre-heat treatment temperature. The structural parameters of cellulose-based carbons are summarized in Table S2, Supporting Information. After calculation,[32] the interlayer spacing (d_{002}) of the carbon materials is 0.358, 0.368, 0.376, and 0.393 nm, corresponding to HC25-J-1500, HC350-J-1500, HC400-J-1500, and HC600-J-1500, respectively (Figure 2e). Compared with graphite (0.335 nm), the increased interlayer spacing in the samples is beneficial for the insertion and extraction of sodium ions. As indicated by the XRD results, the average interlayer spacing d_{002} initially increases

with increasing pretreatment temperature, reaching a maximum of 600 °C (0.393 nm), indicating the highest degree of topological defects and disordered structure. To further investigate the evolution of the crystalline phase with increasing pre-heat treatment temperature, the (002) peaks were simulated using a profile-fitting process (Figure 2d).[33] By calculating the *d*-spacing value (extremely disordered > 0.40 nm, pseudo-graphitic 0.36–0.40 nm, and graphite-like < 0.36 nm), each component of the fitting peaks is allocated to a distinct carbon phase.[34] In comparison with the other samples, HC600-J-1500 exhibited the highest proportion of disordered carbon (56.8%) and the lowest percentages of graphite-like carbon (22.1%) and pseudo-graphitic carbon (21.1%). The impact of pre-heat treatment on the structure of HC materials at high temperatures is also evident from the Raman spectra shown in Figure 2f. The intensity ratio of the 2*D* and *G* bands indicated that the HC25-J-1500 mainly consisted of graphite-like structures,[35] which agree with the TEM results above. The intensity ratio of the 2*D* and *G* bands of HC prepared after pre-heat treatment is gradually reduced compared to HC25-J-1500, indicating a decrease in graphitic carbon, which is consistent with XRD results. Raman spectra of HCs are divided into five peaks ranging from 1000–2000 cm^{-1} (Figure S4, Supporting Information). The peaks positioned at 1580, 1350, 1620, 1500, and 1200 cm^{-1} are assigned to *G*, D_1, D_2, D_3 and D_4 bands, respectively.[4b,10] The intensity ratio of D_1 band/*G* band (I_{D1}/I_G) is related to the defect degree of carbon.[33a] As indicated in Table S2 (Supporting Information), the value of I_{D1}/I_G increases from 1.64 for HC25-J-1500 to 2.40 for HC600-J-1500 (Figure S4, Supporting Information). The evolution of the carbon microstructure indicates that the pre-heat treatment temperature has a significant influence on the formation process of the final carbon structure. Pre-heat treatment transforms vulnerable cellulose into a high-carbonizability framework that is resistant to over-graphitization, slowing the uniform growth of carbon crystals. Besides, this phenomenon indicates that the defect concentration in carbon materials can be regulated by pre-heat treatment temperature. Therefore, the pre-heat treatment plays a crucial role in the growth and accumulation of crystal structure during the FJH process.

The pore structures were first investigated by N_2 adsorption-desorption experiments (Figure S5, Supporting Information). Based on the isotherms, the calculated Brunauer-Emmett-Teller (BET) specific surface area (S_{BET}) of HC600 is measured to be 266 $m^2\ g^{-1}$, a significant increase compared to that of HC25 (2 $m^2\ g^{-1}$) (Figure 2g). After FJH treatment at 1500 °C, the corresponding value of HC600-J-1500 is significantly reduced to 3 $m^2\ g^{-1}$. This result indicates that the open pores formed during the pre-heat treatment process underwent a transformation after FJH, resulting in an inability for N_2 to access. In this case, to determine pore structure within an HC material, the true density and SAXS were tested (Figure 2h–j).[6b,33a,36] Internal closed pore volume can be estimated using the calculation equation ($V_{Close\ Pore} = 1/\rho_{ture\_} 1/2.26$) (Figure 2h).[36a,37] By calculation, the closed pore volumes of HC25-J-1500 and HC600-J-1500 are 0.011 and 0.089 $cm^3\ g^{-1}$, respectively. SAXS pattern of HC600-J-1500 exhibits a higher intensity than that of HC25-J-1500 in the intermediate *q* region, further confirming it contains a greater number of closed pores (Figure 2i). The derived pore size distribution curves indicate that the predominant pore size of the HC600-J-1500 sample is 1.34 nm, which is larger than that of pristine HC at 1.13 nm (Figure 2j; Figure S6a,b, Supporting Information). The specific surface area associated with the SAXS-fitted specific surface area represents total pores (Figure 2i).[38] Notably, following pre-heat treatment, the surface area of these closed nanopores significantly increases from 60 to 397 $m^2\ g^{-1}$. Besides, the fitted results show that the surface of closed nanopores becomes smoother after pre-heat treatments (Figure S6c,d, Supporting Information).[36a] These results further indicate that the open pores formed during the pre-heating process were transformed into closed pores.[11,36a,37,39] Figure 2k illustrates differences in pore structure and size among HC25-J-1500, HC600, and HC600-J-1500. Under other pre-heating process conditions, a corresponding trend is also observed (Figures S7 and S8, Supporting Information).

2.2. Influence of FJH Treatment on Closed-Pore Formation of Hard Carbon

To investigate how carbonization temperature influences the microstructures of HCs, HC600 was selected as the carbon precursor. The HRTEM images in **Figure 3**a,b reveal that the microstructures of HC600-J-1000 and HC600-J-2000 consist of closed pores enclosed by intricately curved nanographitic nanosheets, resembling the structure observed in HC600-J-1500. With the rise in FJH temperature, the size of closed pores increases significantly. Simultaneously, the short-range ordered lattice fringes of pseudographitic domains gradually transform into more defined graphite-like microcrystal stripes, accompanied by a reduction in defects. This progression is further confirmed by the SAED patterns, which demonstrate a clear evolution from blurred to sharp diffraction rings, indicating an increasingly ordered structure in the HCs.[40]

The XRD patterns, presented in Figure S9a (Supporting Information), reveal broad diffraction peaks for the (002) plane at ≈24° and the (100) plane at ≈43°, indicating the non-graphitized structure of HCs. As shown in Figure S9b (Supporting Information), the content of graphite-like carbon increases with higher FJH temperatures. Furthermore, Figure 3c demonstrates that with rising FJH temperature, the (002) peak for HC600-J-1000, HC600-J-1500, and HC600-J-2000 shifts to higher angles, while the calculated $d_{(002)}$ values progressively decrease. This reduction in interlayer spacing reflects enhanced graphitization and improved structural ordering of HCs.[26] The development of the crystal structure of the HCs can also be observed from the Raman spectra in Figure S10a (Supporting Information). HCs generally exhibit broad 2D signals at ≈2700 cm^{-1}, which provide information regarding graphitic layer stacking and coherence. Furthermore, a 2D signal appears with the FJH temperature increasing, implying that some graphitic layer coherence is developing. The values of I_{D1}/I_G are 3.04, 2.40, and 1.74 for HC600-J-1000, HC600-J-1500, and HC600-J-2000 (Figure S10b, Table S2, Supporting Information and Figure 3c), respectively, showing that higher pyrolysis temperature leads to fewer defects.[40]

Based on the N_2 adsorption-desorption isotherms (Figure 3d; Figure S11, Supporting Information), the calculated S_{BET} is calculated to be 11, 3, and 2 $m^2\ g^{-1}$ for HC600-J-1000,

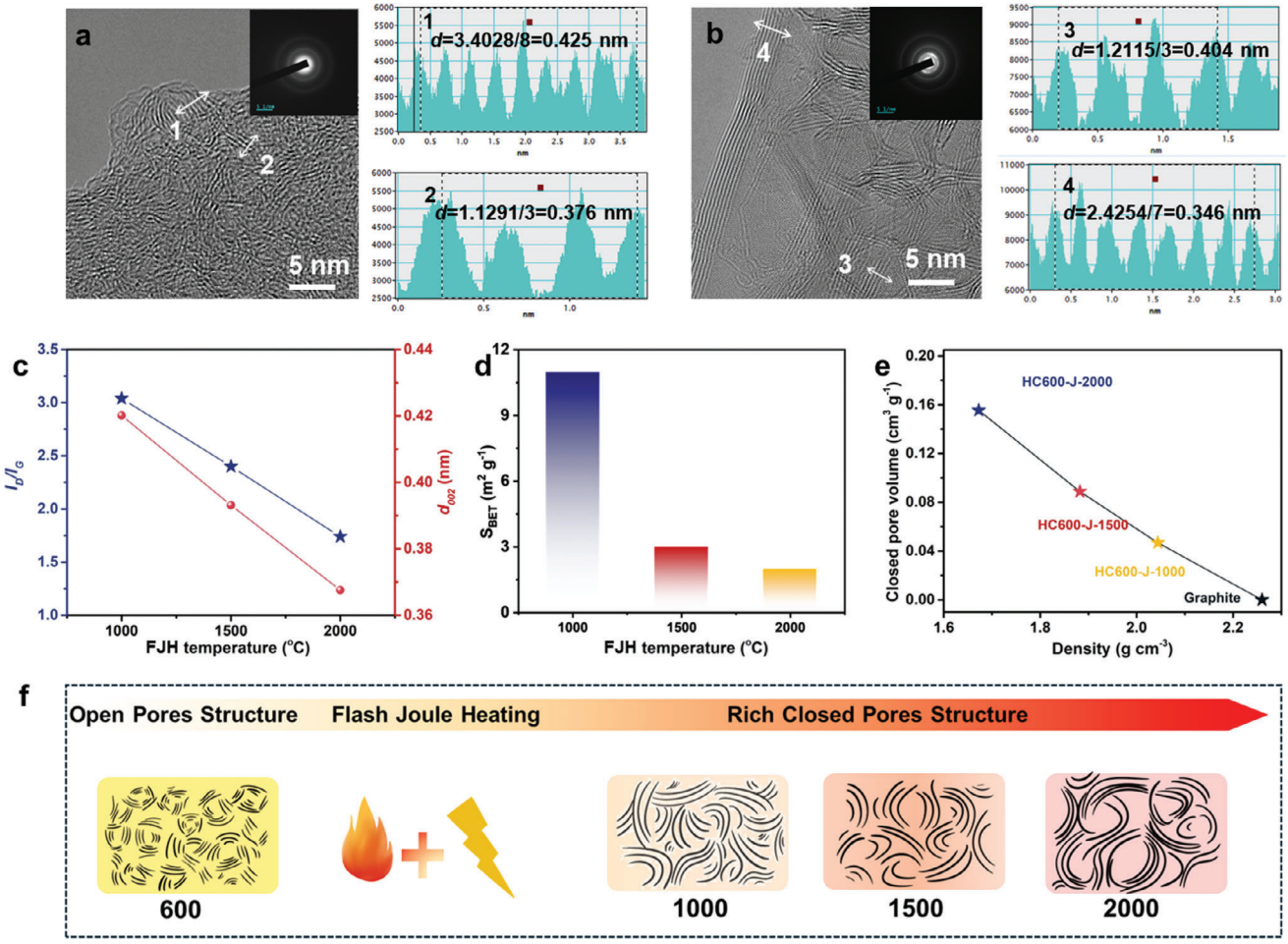

Figure 3. HRTEM and corresponding SEAD images of a) HC600-J-1000 and b) HC600-J-2000. c) d_{002} and I_{D1}/I_G from XRD and Raman spectra fitting curves. d) Value of S_{BET}, e) true density, and the corresponding closed pore volume of HC600-J-1000, HC600-J-1500, and HC600-J-2000. f) Formation mechanism of closed pores in HCs by FJH treatment.

HC600-J-1500, and HC600-J-2000, respectively. The increased carbonization temperature caused the contraction of open pores.[6a,41] The true density values and the obtained closed pore volume are 2.044 g cm^{-3} with 0.047 cm^3 g^{-1}, 1.882 g cm^{-3} with 0.089 cm^3 g^{-1} and 1.673 g cm^{-3} with 0.155 cm^3 g^{-1} for HC600-J-1000, HC600-J-1500 and HC600-J-2000, respectively (Figure 3e, Figures S12–S14, Supporting Information). As shown in Figure S12 (Supporting Information), with pyrolysis temperature rising, the peak strength of ≈0.1 $Å^{-1}$ in SAXS curves increases, indicating an increase in the average radius of closed pores, from 1.34 nm for HC600-J-1500 to 3.43 nm for HC600-J-2000. Higher FJH temperatures promote the shift and folding of graphite-like layers, resulting in more closed pores and being surrounded by multiple parallel carbon layers for sodium storage; however, too high temperatures increase graphite-like carbon content in carbons while narrowing and shrinking the carbon skeleton minimizes closed pores which are not conducive to sodium storage. Therefore, selecting an appropriate FJH carbonization temperature is crucial, as it significantly influences the pore structure of cellulose-derived HC. With temperatures rising, some curved carbon layers tend to fold and form more closed pores. However, excessively high temperatures also promote the migration, stacking, and growth of graphite layers, leading to the shrinkage of closed pores (Figure 3f).

In addition, to emphasize the advantage of FJH treatment, it is compared with HC600-F-1500 using furnace heating at the same carbonization temperature. The closed pore volume of HC600-J-1500 is higher than that of HC600-F-1500, indicating that FJH treatment produces more closed pores than furnace heating treatment (Figure S15, Supporting Information).

2.3. Pre-Heat Treatment Influence on Electrochemical Performance of Hard Carbon

The electrochemical behavior of sodium storage was investigated in a half-cell using sodium metal as the counter/reference electrode. The initial galvanostatic charge/discharge (GCD) curves of HC25-J-1500 and HC600-J-1500 at a current density of 25 mA g^{-1} are depicted in **Figure** 4a. HC600-J-1500 delivers a much higher initial reversible capacity of 362 mAh g^{-1} and an ICE of 92.4% in comparison to HC25-J-1500 (142 mAh g^{-1} and 64.7%).

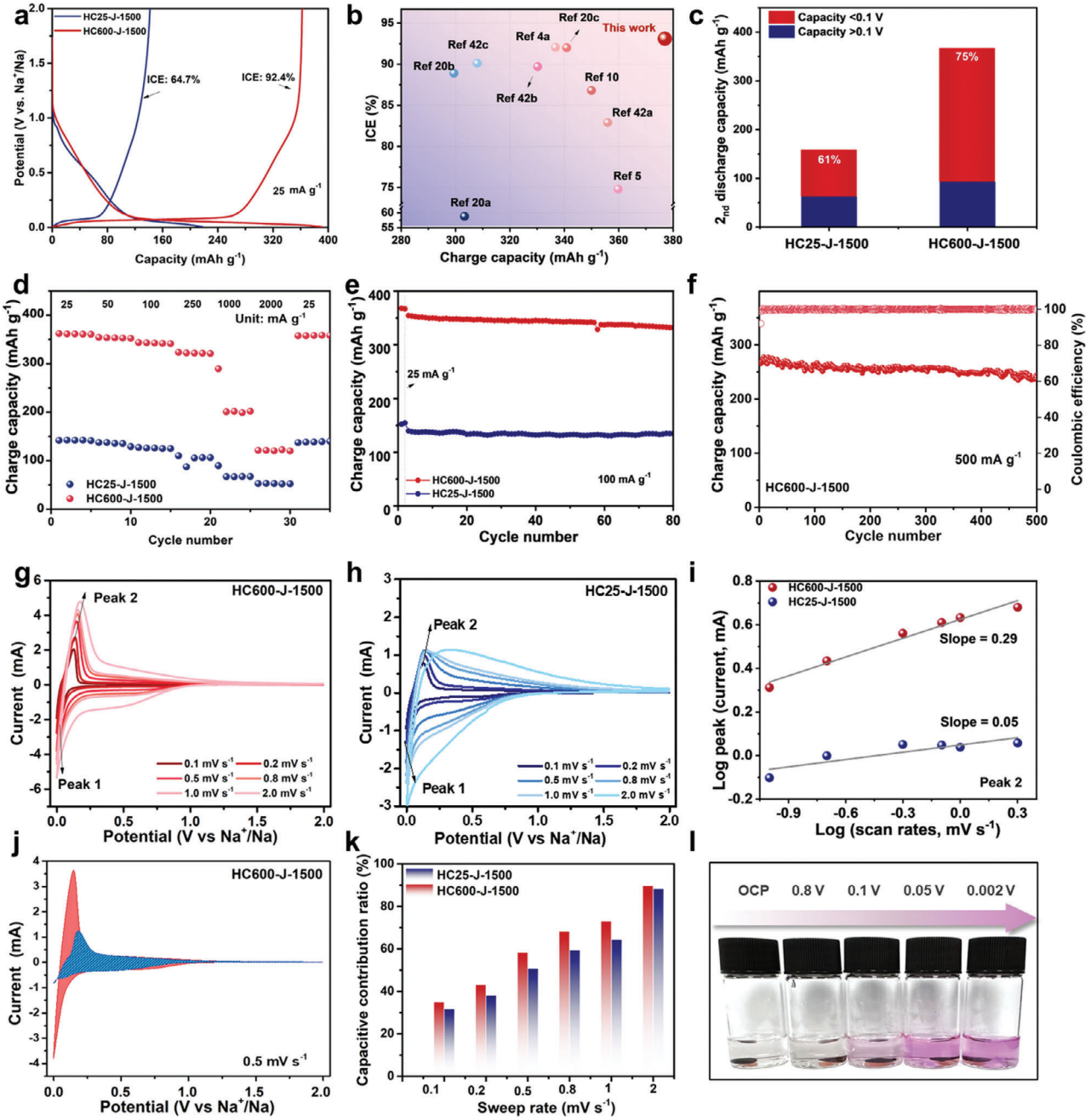

Figure 4. a) The initial GCD curves for HC25-J-1500 and HC600-J-1500 anodes at 25 mA g^{-1}. b) Comparison of the ICE and specific capacity with the previously reported HCs.[4a,5,10,20a–c,42] c) The second discharge capacity of samples contributed from the slope and plateau region of HC25-J-1500 and HC600-J-1500. d) Rate performance of HC25-J-1500 and HC600-J-1500. e) Cycling performance of HC25-J-1500 and HC600-J-1500 at 100 mA g^{-1}. f) Cycling stability of HC600-J-1500 at the current density of 500 mA g^{-1}. CV curves of g) HC600-J-1500 and h) HC25-J-1500 anodes at various scanning rates from 0.1 to 2 mV s^{-1}. i) The corresponding correlations between peak current (*i*) and scan rate (*v*) for peak 2. j) Capacitive contribution percentage of HC600-J-1500 at 0.5 mV s^{-1} scanning rates. k) Capacitive contribution percentage of HC600-J-1500 and HC25-J-1500 at various scanning rates. l) The color changes of ethanol containing 1% phenolphthalein after reaction with HC600-J-1500 at different potentials.

To ensure reproducibility, we tested five independently prepared batteries using HC600-J-1500 as the active material. The first-cycle charge capacities were 362, 364, 360, 366, and 368 mAh g^{-1}, with an average of 364 mAh g^{-1}. The corresponding ICE values were 92.4%, 92.2%, 92.9%, 92.6%, and 93.1%, with an average of 92.6%. The data is shown in Figure S16 (Supporting Information) where error bars represent the standard deviation, demonstrating the reproducibility of the observed performance. Notably, the ICE value is superior to the majority of reported HC anodes, even those with similar carbonization temperatures (Figure 4b; Table S3, Supporting Information).[4a,5,10,20a–c,42] Similar to previously reported HC materials, the HCs electrodes

exhibit typical discharge–charge curves; a sloping voltage region above 0.10 V and a plateau region below 0.10 V. The plateau discharge capacities of HC25-J-1500 and HC600-J-1500 show significant differences. From Figure 4c, the plateau discharge capacity HC600-J-1500 (276 mAh g^{-1}) is ≈2.9 times that of HC25-J-1500 (96 mAh g^{-1}). The high plateau capacity of HC600-J-1500 can be attributable to its abundant closed pores, which have been identified as suitable sites for Na storage.[43] The plateau capacity varies with the closed pore content in other HCs electrodes as well (Figure S17, Supporting Information). Based on the above discussion, the closed pore structure in HC plays a key role in the plateau capacity contribution. Apart from these, the rate capability of HC600-J-1500 and HC25-J-1500 by applying stepwise current densities ranging from 25 to 2000 mA g^{-1} also show significant distinction (Figure 4d and Figure S18, Supporting Information). HC600-J-1500 electrode shows a much higher rate capability than that of HC25-J-1500, with a specific capacity of 323 mAh g^{-1} at 250 mA g^{-1}. This indicates that the closed-pore characteristics resulting from the ultramicroporous structure formed during pre-heat treatment have a positive impact on rate performance. Furthermore, the rate performance of HC600-J-1500 exhibits higher capacity compared to other samples pre-heat at other temperatures (Figure S19, Supporting Information). Both HCs show excellent cycling stability (Figure 4e). In particular, even at a current density of 500 mA g^{-1}, HC600-J-1500 still maintains a capacity of 236 mAh g^{-1} after 500 cycles and the retention rate is maintained at 89.0% when compared to the capacity of the third cycle (Figure 4f).

To further understand the sodium storage behavior, cyclic voltammetry (CV) curves at different scan rates were recorded to analyze the reaction kinetics (Figure 4g,h). It is observed that the peak current of HC600-J-1500 increases with the scan rate more intensively than that of the HC25-J-1500 electrode. Based on the relationship ($i = av^b$) between peak current (i) and scan rate (v), b values for peak 2 in HC600-J-1500 is 0.29, which is higher than that of HC25-J-1500 (0.05) (Figure 4i). This means that the pre-heat treatment has a significant impact on electrochemical kinetic processes. Furthermore, fitting results from differentiating currents contributed by surface-controlled processes and diffusion-controlled reactions illustrate that the sloping region is mainly dominated by surface-controlled currents while diffusion-controlled currents account for the plateau region (Figure 4j,k). The product CH_3CH_2ONa from Na and ethanol reaction can turn phenolphthalein solution red, and thus the phenolphthalein color test is used to prove the presence of quasi-metallic Na in the closed pores.[44] Obviously, the color of the ethanol solution of HC600-J-1500 gradually deepened as the potential decreased (Figure 4i).

2.4. Influence of FJH Treatment on Electrochemical Performance of Hard Carbon

In order to investigate the influence of FJH treatment, including key parameters such as carbonization temperature, carbonization methods, and pulse widths, we conducted a systematic study to evaluate their effects on the electrochemical performances of HC. Using HC600 as the precursor, we adjusted the FJH parameters to set carbonization temperatures at 1000 °C, 1500 °C, and 2000 °C, resulting in the preparation of HC600-J-1000, HC600-J-1500, and HC600-J-2000. As shown in **Figure 5a**, HC600-J-1500 demonstrates the highest charge capacity and ICE in the first cycle (362 mAh g^{-1} and 92.4%) compared to HC600-J-1000 (258 mAh g^{-1} and 87.1%) and HC600-J-2000 (323 mAh g^{-1} and 88.3%). With increasing FJH temperature, the plateau charge capacity ratio in the second cycle also rises, reaching 57.7% (151 mAh g^{-1}) for HC600-J-1000, 75.3% (276 mAh g^{-1}) for HC600-J-1500, and 89.6% (293 mAh g^{-1}) for HC600-J-2000 (Figure 5b). This trend is attributed to the formation of a greater number of closed pores, which are widely recognized as highly effective storage sites for Na^+ ions.[8,21] When the pulse width is extended to 20 s (denoated as HC600-J-1500-20S), the reversible capacity and ICE are further improved, reaching 377 mAh g^{-1} and 93.3% (Figure S20, Supporting Information), which is as far as we know a breakthrough in regulating structures of HC by FJH process. However, the energy consumption increases ≈20-fold under this condition, making HC600-J-1500 the more economical choice in terms of energy efficiency. The Na ion storage performanes of using FJH and conventional furnace heating, were further studied. As shown in Figure S21a (Supporting Information), the initial reversible capacity of HC prepared by FJH is significantly higher than that achieved by furnace heating (denoted as HC600-F-1500, 296 mAh g^{-1}). Additionally, Figure S21b (Supporting Information) illustrates that the plateau capacity of HC600-J-1500 exceeds that of HC600-F-1500. This disparity may stem from the differences in the carbonization process. Traditional furnace heating provides sufficient time for carbon layer rearrangement to occur, as suggested by prior studies.[45] In contrast, the rapid heating and cooling characteristic of FJH treatment preserves more of the precursor's microscopic morphology, resulting in a higher number of closed pores. The HC600-J-1500 electrode shows better rate capability than that of HC600-J-1000 and HC600-J-2000 (Figure 5c). Besides, the rate performance of HC600-J-1500 exhibits higher capacity compared to that of HC600-F-1500 (Figure S22, Supporting Information).

To further understand FJH treatment influence on the sodium storage behavior, CV curves at different scan rates were recorded to analyze the reaction kinetics (Figures S23 and S24, Supporting Information). It is observed that the peak currents of HC600-J-1500 increase more intensively with the scan rate than those of the HC600-J-2000 electrode, but the increasement becomes weak as compared to that of HC600-J-1000. Based on the relationship ($i = av^b$) between peak current (i) and scan rate (v), b values for peaks 1 and 2 in HC600-J-1500 are 0.34 and 0.29, which are higher than those for HC600-J-2000 (0.25 and 0.16) and lower than those for HC600-J-1000 (0.42 and 0.38) (Figure S24d,e, Supporting Information). This means that the lower carbonization temperature is conducive to the fast kinetics while excessively high temperatures impede the ion transpot/diffusion. Furthermore, fitting results from differentiating currents contributed by surface-controlled processes and diffusion-controlled reactions illustrate that the sloping region is mainly dominated by surface-controlled currents while diffusion-controlled currents account for the plateau region (Figure 5d). This further confirms the quasi-metallic sodium formed at the end of the discharge process and the Na storage mechanism based on closed pore filling.[43a] To further evaluate the diffusion capability of sodium ions in the electrode material, the galvanostatic

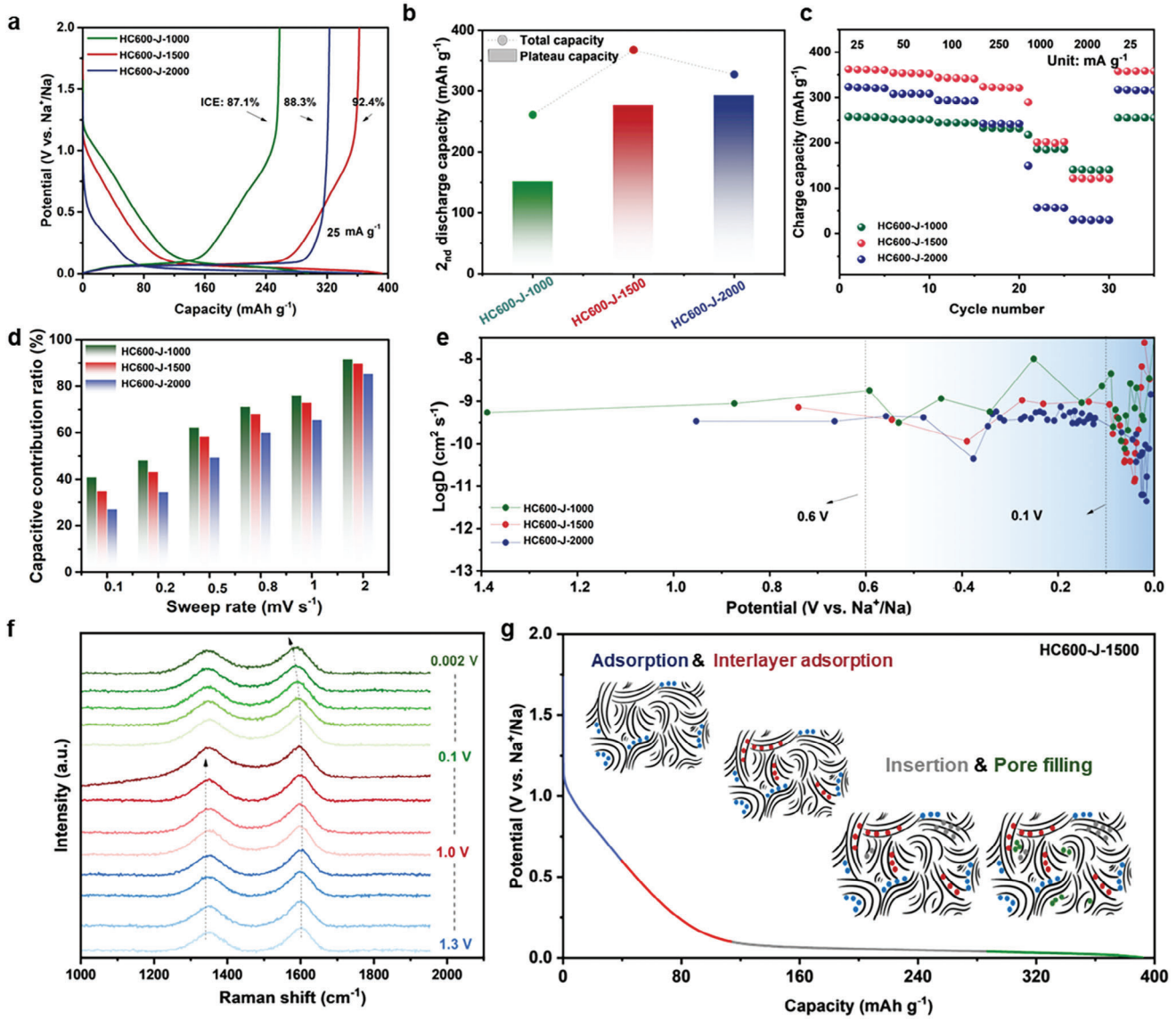

Figure 5. a) The initial GCD curves for HC600-J-1000, HC600-J-1500, and HC600-J-2000 at 25 mA g^{-1}. b) Discharge capacity of samples contributed from slope and plateau region of HC600-J-1000, HC600-J-1500, and HC600-J-2000 in 2nd cycle. c) Rate performance of HC600-J-1000, HC600-J-1500, and HC600-J-2000. d) Capacitive contribution percentage of HCs at various scanning rates. e) Na^+ diffusion coefficients during the sodiation process for HC600-J-1000, HC600-J-1500, and HC600-J-2000. f) In situ Raman spectra of HC600-J-1500 electrode during the discharge process. g) Schematic diagram at various Na^+ storage stages for HCs anode.

intermittent titration technique (GITT) was performed, and the diffusivity coefficient (D_{Na+}) was calculated. The resulting GITT curves, along with the corresponding calculated D_{Na+} values, are presented in Figure S25 (Supporting Information) and Figure 5e, respectively. The D_{Na+} of all samples shows less fluctuations with a potential >0.1 V during the sodiation process, corresponding to the adsorption-dominated Na^+ storage behavior. After that, D_{Na+} of HCs declines rapidly at first and rises later within 0.1 to 0.002 V, mainly ascribed to the Na^+ intercalation and nanoclusters formation in the closed pores, respectively. It is evident that the closed pore volume is positively correlated with the plateau capacity; in other words, carbon samples with more closed pores have higher plateau capacity.[46] In addition, as the FJH temperature increases, the potential of minimum value of D_{Na+} shifts towards a lower direction, which has also been observed in the CV curves (Figure S26, Supporting Information). This is related to the carbon layers that are curled and intertwined outside the closed pores. The interlayer spacing of HC600-J-1500 is smaller than that of HC600-J-1000 but larger than that of HC600-J-2000, which is suitable for the transport and storage of Na ions. Based on the above findings, the Na^+ storage mechanism for HCs can be summarized by emphasizing the relationship between its microstructures and electrochemical performance. As shown by the *in-situ* Raman shifts in Figure 5f, from the open circuit potential to 1.0 V, the positions and intensities of the G and D bands remain stable, indicating that sodium storage during this stage

primarily involves adsorption. As the potential further decreases to 0.1 V, the G band in the Raman spectra begins to exhibit a slight redshift, possibly indicating the gradual migration of sodium ions from surface adsorption to interlayer adsorption within the carbon structure,[5] in line with the some fluctuations of D_{Na+} in range around 0.1-0.6 V in Figure 5e. Below 0.1 V, the similar redshift in the G-band peak suggestes sodium insertion into the HC layers. This insertion occupies the $\pi*$ anti-bonding orbitals, leading to an extension of the C–C bonds.[11] As depicted in Figure 5g, a large number of Na^+ ions are initially adsorbed on the surface or defect structures of HC600-J-1500 at potentials ranging from ≈0.6 to 2.0 V. Subsequently, the Na ions are adsorbed on the edge of graphite interlayer ≈0.1 to ≈0.6 V, followed by their insertion into the graphite interlayer and gradual filling of the inner surfaces below 0.1 V. Upon further discharging, sodium metal clusters are formed through sodium-sodium interactions, aggregating to nucleate and store in size-suitable closed pore structures.[4a,33a,47] Based on the above findings, full cells consisting of commercial $Na_3V_2(PO_4)_3$ and HC600-J-1500 as cathode and anode materials were tested at 0.1 C in a potential range of 1.5–3.8 V to demonstrate the practical feasibility of using Na/HC600-J-1500 for applications. As shown in Figure S27 (Supporting Information), the discharge-specific capacity of the assembled cell reaches 327 mAh g^{-1} at a current density of 0.1 C (based on the active material mass of the anode electrode).

3. Conclusion

We have developed an effective strategy for closed-pore regulation by a facile pre-heat and FJH treatment for biomass-derived HCs. The pre-heat treatment can format ultramicropores, which transform vulnerable cellulose into a high-carbonizability framework, enhancing the final yield of biomass-derived HCs. The FJH-enriched closed pores are rapidly created from the ultramicropores surrounded by the walls derived from a high-carbonizability framework, with expanded interlayer spacings as accessible Na^+ channels. Moreover, this carbon phase regulation technology can be extended to various biomass feedstocks, demonstrating its remarkable versatility. The high-performance HC anode exhibits high ICE (93.3%) and charge capacity (377 mAh g^{-1}). The HC sodium storage mechanism has been verified to be a mode of "adsorption-interlayer adsorption-insertion-pore filling formation". This research paves the way for the design and synthesis of biomass-derived HCs with customizable sodium storage mechanisms toward high-performance SIBs.

4. Experimental Section

Material and Methods: Microcrystalline cellulose was provided by Pingju Biotechnology Group Co., Ltd. (Shandong, China) with a purity of 99%. The crystallinity of the microcrystalline cellulose was determined to be 85.7% using the Segal peak height method.[23] The powder obtained was processed for carbonization using two separate techniques: firstly, heating in a tube furnace at 350, 400, 600, and 800 °C for 3 h with a heating rate of 5 °C min^{-1} (denoted as HC300, HC400, HC600, and HC800), and the furnace heating was conducted under a nitrogen atmosphere with a flow rate of 80 mL min^{-1} to prevent oxidation of samples. In the FJH process, the precursor powder is lightly compressed within a carbon tube positioned between two carbon electrodes (Figure S28, Supporting Information). The FJH reactor (Hefei In situ Technology Co., Ltd.) applies high-voltage electrical pulses, generating ultrahigh heating rates and temperatures. This enables ultrafast carbonization within approximately a few seconds to reach 1000, 1500, or even 2000 °C (denoted as HC*xx*-J-1000, HC*xx*-J-1500, and HC*xx*-J-2000) significantly outpacing the capabilities of most conventional furnaces. HC600-F-1500 was prepared by heating HC600 in a tube furnace at 1500 °C for 3 h under an argon atomosphere with a heating rate of 2 °C min^{-1}.

Structural Characterization: The morphology and texture were obtained using a TEM (JEOL JEM-F200, 200 kV) equipped with SAED. The microcrystal structures of materials were characterized by XRD measurements (Bruker D8 Advance; Cu Ka radiation, 0.154 nm) at room temperature. TGA measurement was performed on a Mettler TGA/DSC1 analyzer from room temperature to 800 °C at a rate of 10 °C min^{-1} in a nitrogen atmosphere. Raman spectra were carried out on a Renishaw inVia Laser Micro-Raman Spectrometer excited by a 532 nm He-Ne laser with a laser spot size of 1 mm and a laser power of 10%. In situ Raman measurements were performed using a custom-built setup, as shown in Figure S29, Supporting Information. Pore structure information (specific surface areas, pore-size distributions) was collected following a Micromeritics ASAP 2460 surface area and porosity analyzer. Before measurement, the samples were degassed overnight at 250 °C for HCs and at 120 °C for HC25, HC350, HC400, and HC600. SAXS from a Xenocs Xeuss 2.0 with a Ni-filtered Cu Kα source. True density data were collected by Ultrapyc 3000 using helium as analysis gas. The true density of the materials was measured using a helium pycnometer (as shown in Figure S30, Supporting Information), and here helium was chosen as the probing gas due to its ability to penetrate the smallest accessible voids.

Electrochemical Measurements: The original working electrodes were fabricated by confusing HCs as active materials with sodium alginate as a binder at a weight of 95:5 in deionized water and then slurry coating on Cu foils. After drying at 80 °C overnight, the electrodes were cut into a 10 mm diameter circle with an average areal loading of ≈1.5–2.5 mg cm^{-2}. The electrochemical performances were carried out in standard CR2032 coin cells by using metallic Na as a counter electrode, glass fibers separator from Whatman, and 1.0 mol L^{-1} $NaPF_6$ in diglyme solution as the electrolyte. The $Na_3V_2(PO_4)_3$ cathode was prepared by mixing with polyvinylidene fluoride and Super P in a weight ratio of 8:1:1, dissolved in N-methyl-2-pyrrolidone solvent, and coated onto the Al foil substrate. The coin full-cells were conducted within a potential range of 1.5–3.8 V with the N/P ratio of 0.95. The GCD cycles were carried out on the LAND-CT2001A battery test system from 0.002 to 2 V. versus Na^+/Na. CV tests with various scan rates were measured by a multichannel Electrochemical Workstation (Bio-logic VMP3). The phenolphthalein color test using 3 mL 1% phenolphthalein after reaction with HC600-J-1500 at different potentials. GITT testing was performed by a Land battery system with a constant discharge–charge current density of 25 mA g^{-1} for 30 min duration followed by an interval of 180 min as one step within a potential range of 0.002–2.0 V, then charged in the same way.

Supporting Information

Supporting Information is available from the Wiley Online Library or from the author.

Acknowledgements

This work was supported by the National Natural Science Foundation of China (52322203, 52473220), the Key Research and Development Program of Shaanxi Province (2024GH-ZDXM-21), the Fundamental Research Funds for the Central Universities, and the Shaanxi Science and Technology Innovation Team (2023-CX-TD-44).

Conflict of Interest

The authors declare no conflict of interest.

Data Availability Statement

The data that support the findings of this study are available from the corresponding author upon reasonable request.

Keywords

closed pores, flash Joule heating, hard carbons, pre-heat treatments, sodium-ions

Received: December 1, 2024
Revised: January 19, 2025
Published online:

[1] a) Y. Li, Y. X. Lu, P. Adelhelm, M. M. Titirici, Y. S. Hu, *Chem. Soc. Rev.* **2019**, *48*, 4655; b) F. Wang, Z. Jiang, Y. Zhang, Y. Zhang, J. Li, H. Wang, Y. Jiang, G. Xing, H. Liu, Y. Tang, *eScience*. **2024**, *4*, 100181; c) Y. Gao, H. Zhang, J. Peng, L. Li, Y. Xiao, L. Li, Y. Liu, Y. Qiao, S. L. Chou, *Carbon Energy*. **2024**, *6*, e464; d) Y. Y. Zhu, Y. H. Wang, Y. T. Wang, T. J. Xu, P. Chang, *Carbon Energy*. **2022**, *4*, 1182.

[2] a) L. Kitsu Iglesias, E. N. Antonio, T. D. Martinez, L. Zhang, Z. Zhuo, S. J. Weigand, J. Guo, M. F. Toney, *Adv. Energy Mater.* **2023**, *13*, 2302171; b) H. L. Sun, Q. Y. Zhang, Y. Q. Ma, Z. J. Li, D. Zhang, Q. J. Sun, Q. J. Wang, D. Liu, B. Wang, *Energy Storge Mater.* **2024**, *67*, 103269.

[3] G. Huang, H. Zhang, F. Gao, D. Zhang, Z. Zhang, Y. Liu, Z. Shang, C. Gao, L. Luo, M. Terrones, Y. Wang, *Carbon*. **2024**, *228*, 119354.

[4] a) J. Zhao, X. X. He, W. H. Lai, Z. Yang, X. H. Liu, L. Li, Y. Qiao, Y. Xiao, L. Li, X. Wu, S. L. Chou, *Adv. Energy Mater.* **2023**, *13*, 2300444; b) X. X. He, W. H. Lai, Y. Liang, J. H. Zhao, Z. Yang, J. Peng, X. H. Liu, Y. X. Wang, Y. Qiao, L. Li, X. Wu, S. L. Chou, *Adv. Mater.* **2023**, *35*, 2302613; c) J. Liu, Y. You, L. Huang, Q. Zheng, Z. Sun, K. Fang, L. Sha, M. Liu, X. Zhan, J. Zhao, Y. C. Han, Q. Zhang, Y. Chen, S. Wu, L. Zhang, *Adv. Mater.* **2024**, *36*, 2407369; d) F. Xu, Y. Q. Qiu, H. J. Han, G. S. Jiang, R. X. Zhao, E. Zhang, H. J. Li, H. Q. Wang, S. Kaskel, *Carbon*. **2020**, *159*, 140.

[5] D. Sun, L. Zhao, P. L. Sun, K. Zhao, Y. K. Sun, Q. Zhang, Z. C. Li, Z. Ma, F. Z. Zheng, Y. Yang, C. B. Lu, C. Peng, C. M. Xu, Z. H. Xiao, X. L. Ma, *Adv. Funct. Mater.* **2024**, *34*, 2403642.

[6] a) Y. Q. Li, Y. X. Lu, Q. S. Meng, A. C. S. Jensen, Q. Q. Zhang, Q. H. Zhang, Y. X. Tong, Y. R. Qi, L. Gu, M. M. Titirici, Y. S. Hu, *Adv. Energy Mater.* **2019**, *59*, 25; b) D. K. Liu, Y. Q. Qiu, Y. X. Du, J. Y. Yang, X. H. Jing, X. Peng, Q. Song, F. Xu, *J. Mater. Chem. A.* **2024**, *12*, 16695.

[7] a) Q. Li, X. S. Liu, Y. Tao, J. X. Huang, J. Zhang, C. P. Yang, Y. Zhang, S. Zhang, Y. B. Jia, Q. Lin, Y. Xiang, J. Cheng, W. Lv, F. Kang, Y. Yang, Q. H. Yang, *Nat Sci Rev.* **2022**, *9*, nwac084; b) X. Chen, N. Sawut, K. Chen, H. Li, J. Zhang, Z. Wang, M. Yang, G. Tang, X. Ai, H. Yang, Y. Fang, Y. Cao, *Energy Environ. Sci.* **2023**, *16*, 4041.

[8] A. Kamiyama, K. Kubota, D. Igarashi, Y. Youn, Y. Tateyama, H. Ando, K. Gotoh, S. Komaba, *Angew Chem Int Edit.* **2021**, *60*, 5114.

[9] C. Wu, Y. Yang, Y. Zhang, H. Xu, W. Huang, X. He, Q. Chen, H. Dong, L. Li, X. Wu, S. Chou, *Angew Chem Int Edit.* **2024**, *63*, 202406889.

[10] Y. Wang, Z. Yi, L. Xie, Y. Mao, W. Ji, Z. Liu, X. Wei, F. Su, C. M. Chen, *Adv. Mater.* **2024**, *36*, 2401249.

[11] Z. Zheng, S. Hu, W. Yin, J. Peng, R. Wang, J. Jin, B. He, Y. Gong, H. Wang, H. J. Fan, *Adv. Energy Mater.* **2023**, *14*, 2303064.

[12] a) F. B. Yu, C. Jia, X. Wu, L. M. Sun, Z. J. Shi, T. Teng, L. T. Lin, Z. L. He, J. Gao, S. C. Zhang, L. Wang, S. B. Wang, X. D. Zhu, *Nat Commun.* **2023**, *14*, 4975; b) B. Deng, L. Eddy, K. M. Wyss, C. S. Tiwary, J. M. Tour, *Nat. Rev. Clean Technol.* **2025**, *1*, 32.

[13] C. Wang, W. Ping, Q. Bai, H. Cui, R. Hensleigh, R. Wang, A. H. Brozena, Z. Xu, J. Dai, Y. Pei, C. Zheng, G. Pastel, J. Gao, X. Wang, H. Wang, J. C. Zhao, B. Yang, X. R. Zheng, J. Luo, Y. Mo, B. Dunn, L. Hu, *Science*. **2020**, *368*, 521.

[14] J. Chen, Y. Ma, T. Huang, T. Jiang, S. Park, J. Xu, X. Wang, Q. Peng, S. Liu, G. Wang, W. Chen, *Adv. Mater.* **2024**, *36*, 2312369.

[15] D. X. Luong, K. V. Bets, W. A. Algozeeb, M. G. Stanford, C. Kittrell, W. Chen, R. V. Salvatierra, M. Ren, E. A. Mchugh, P. A. Advincula, Z. Wang, M. Bhatt, H. Guo, V. Mancevski, R. Shahsavari, B. I. Yakobson, J. M. Tour, *Nature*. **2020**, *577*, 647.

[16] a) P. Du, B. Deng, X. He, W. Zhao, H. Liu, Y. Long, Z. Zhang, Z. Li, K. Huang, K. Bi, M. Lei, H. Wu, *ACS Nano*. **2024**, *19*, 1327; b) Y. C. Yin, C. Li, X. Hu, D. Zuo, L. Yang, L. Zhou, J. Yang, J. Wan, *ACS Energy Lett.* **2023**, *8*, 3005.

[17] a) X. Yao, S. Chen, C. Wang, T. Chen, J. Li, S. Xue, Z. Deng, W. Zhao, B. Nan, Y. Zhao, K. Yang, Y. Song, F. Pan, L. Yang, X. Sun, *Adv. Energy Mater.* **2023**, *14*, 2303422; b) W. W. Ping, C. W. Wang, R. L. Wang, Q. Dong, Z. W. Lin, A. H. Brozena, J. Q. Dai, J. Luo, L. B. Hu, *Sci. Adv.* **2020**, *6*, eabc8641

[18] Y. Xu, W. Yuan, C. Geng, Z. Hu, Q. Li, Y. Zhao, X. Zhang, Z. Zhou, C. Yang, Q. H. Yang, *Adv. Sci.* **2024**, *11*, 2402497.

[19] J. Chao, P. Mingyue, L. Yuanda, L. Yize, Z. Minghao, L. Beibei, L. Jiahao, W. Tao, W. Liang, B. Ting, W. Meiling, Y. Fengbo, S. Liming, L. Litao, T. Tao, W. Xuan, H. Zhelin, G. Jie, L. Jiewen, Z. Shicheng, Y. Yi, *One Earth*. **2022**, *5*, 1394.

[20] a) M. Yuan, S. Yu, K. Wang, C. Mi, L. Shen, *Solid State Ion.* **2024**, *414*, 116622; b) Y. Zhen, Y. Chen, F. Li, Z. Guo, Z. Hong, M. M. Titirici, *Proc Natl Acad Sci U S A*. **2021**, *118*, 2111119118; c) Z. Song, Q. Du, J. Chen, J. Huang, Y. Chen, L. Zheng, Z. Huang, H. Dai, Z. Hong, *Chem Eng J*. **2024**, *496*, 154103; d) S. Dong, Y. L. Song, Y. Z. Fang, G. L. Wang, Y. Y. Gao, K. Zhu, D. X. Cao, *ACS Appl. Energy Mater.* **2024**, *7*, 11288.

[21] Z. Tang, R. Zhang, H. Wang, S. Zhou, Z. Pan, Y. Huang, D. Sun, Y. Tang, X. Ji, K. Amine, M. Shao, *Nat. Commun.* **2023**, *14*, 6024.

[22] L. Xiao, H. Lu, Y. Fang, M. L. Sushko, Y. Cao, X. Ai, H. Yang, J. Liu, *Adv. Energy Mater.* **2018**, *8*, 1703238.

[23] K. S. Salem, N. K. Kasera, M. A. Rahman, H. Jameel, Y. Habibi, S. J. Eichhorn, A. D. French, L. Pal, L. A. Lucia, *Chem Soc Rev.* **2023**, *52*, 6417.

[24] M. S. Rana, M. A. Rahim, M. P. Mosharraf, M. F. K. Tipu, J. A. Chowdhury, M. R. Haque, S. Kabir, M. S. Amran, A. A. Chowdhury, *Polymers* **2023**, *15*, 1530.

[25] a) T. Nomura, H. Mizuno, E. Minami, H. Kawamoto, *Energies*. **2021**, *14*, 1842; b) T. Shoji, H. Kawamoto, S. Saka, *J. Anal. Appl. Pyrolysis*. **2017**, *124*, 638.

[26] G. Zhang, C. Chen, C. Xu, J. Li, H. Ye, A. Wang, X. Cao, K. Sun, J. Jiang, *Energy Fuels*. **2024**, *38*, 8326.

[27] a) Z. Wang, B. Pecha, R. J. M. Westerhof, S. R. A. Kersten, C. Z. Li, A. G. Mcdonald, M. Garcia-Perez, *Ind. Eng. Chem. Res.* **2014**, *53*, 2940; b) E. Leng, A. I. Ferreiro, T. Liu, X. Gong, M. Costa, X. Li, M. Xu, *J. Anal. Appl. Pyrolysis*. **2020**, *152*, 104863.

[28] a) W. J. Liu, H. Jiang, H. Q. Yu, *Chem. Rev.* **2015**, *115*, 12251; b) F. Wang, T. Zhang, T. Zhang, T. He, F. Ran, *Nano-Micro Lett.* **2024**, *16*, 148.

[29] W. N. Li, J. F. Li, B. W. Biney, Y. C. Yan, X. P. Lu, H. Li, H. Liu, W. Xia, D. Liu, K. Chen, A. J. Guo, *Energy Storge Mater* **2025**, *74*, 103867.

[30] a) H. He, J. He, H. Yu, L. Zeng, D. Luo, C. Zhang, *Adv. Energy Mater.* **2023**, *13*, 2300357; b) F. Xu, H. J. Han, Y. Q. Qiu, E. Zhang, H. Repich, C. Z. Qu, H. W. Yu, H. Q. Wang, S. Kaskel, *Carbon*. **2020**, *167*, 896.

[31] X. Yu, L. Xin, X. W. Li, Z. Q. Wu, Y. Liu, *Mater. Today*. **2022**, *59*, 25.

[32] Y. Du, Y. Qiu, R. Zhuang, X. Jing, D. Liu, X. Peng, L. Yan, F. Xu, *Carbon*. **2024**, *221*, 118929.

[33] a) M. X. Song, Z. L. Yi, R. Xu, J. P. Chen, J. Y. Cheng, Z. F. Wang, Q. L. Liu, Q. G. Guo, L. J. Xie, C. M. Chen, *Energy Storge Mater.* **2022**, *51*, 620; b) N. Sun, Z. R. X. Guan, Y. W. Liu, Y. L. Cao, Q. Z. Zhu, H. Liu, Z. X. Wang, P. Zhang, B. Xu, *Adv. Energy Mater.* **2019**, *9*, 1901351; c) B.

Cao, H. Liu, B. Xu, Y. Lei, X. Chen, H. Song, *J. Mater. Chem. A.* **2016**, *4*, 6472.
[34] Y. Liu, G. Huang, Y. Li, Y. Yao, Q. Liu, B. Xing, J. Jia, C. Zhang, *Appl. Surf. Sci.* **2021**, *537*, 147824.
[35] Z. Chen, W. Ren, L. Gao, B. Liu, S. Pei, H. M. Cheng, *Nature Mater.* **2011**, *10*, 424.
[36] a) K. Wang, F. Sun, H. Wang, D. Wu, Y. Chao, J. Gao, G. Zhao, *Adv. Funct. Mater.* **2022**, *32*, 2203725; b) Y. Qiu, G. Jiang, Y. Su, X. Zhang, Y. Du, X. Xu, Q. Ye, J. Zhang, M. Ban, F. Xu, H. Wang, *Carbon Energy.* **2024**, *6*, e479.
[37] Q. Meng, Y. Lu, F. Ding, Q. Zhang, L. Chen, Y. S. Hu, *ACS Energy Lett.* **2019**, *4*, 2608.
[38] a) D. Saurel, J. Segalini, M. Jauregui, A. Pendashteh, B. Daffos, P. Simon, M. Casas-Cabanas, *Energy Storge Mater.* **2019**, *21*, 162; b) A. Emmerling, J. Fricke, *J. Non-Crystal Solids.* **1992**, *145*, 113; c) Q. J. Ren, J. Wang, L. Yan, W. J. Lv, F. M. Zhang, L. J. Zhang, B. H. Liu, Z. Q. Shi, *Chem Eng J.* **2021**, *425*, 131656.
[39] X. Zhang, R. Duan, T. J. Zheng, P. T. Chen, X. W. Yu, Z. J. Qiao, D. B. Ruan, *Chem Eng J.* **2024**, *498*, 155232.
[40] X. Zhang, Y. Cao, G. Li, G. Liu, X. Dong, Y. Wang, X. Jiang, X. Zhang, Y. Xia, *Small.* **2024**, *20*, 2311197.
[41] H. Wang, F. Sun, Y. Wang, D. Wu, J. Gao, J. Wang, J. Gao, *Carbon.* **2024**, *229*, 119528.
[42] a) H. Chen, N. Sun, Q. Zhu, R. A. Soomro, B. Xu, *Adv. Sci.* **2022**, *9*, 2200023; b) G. Zhao, T. Xu, Y. Zhao, Z. Yi, L. Xie, F. Su, Z. Yao, X. Zhao, J. Zhang, W. Xie, X. Li, L. Dong, C. M. Chen, *Energy Storge Mater.* **2024**, *67*, 103282; c) Y. Chen, H. Sun, X. X. He, Q. Chen, J. H. Zhao, Y. Wei, X. Wu, Z. Zhang, Y. Jiang, S. L. Chou, *Small.* **2024**, *20*, 2307132.
[43] a) S. Y. Zhou, Z. Tang, Z. Y. Pan, Y. C. Huang, L. Zhao, X. Zhang, D. Sun, Y. G. Tang, A. S. Dhmees, H. Y. Wang, *SusMat.* **2022**, *2*, 357; b) F. Xie, Z. Xu, Z. Guo, A. C. S. Jensen, J. Feng, H. Luo, F. Ding, Y. Lu, Y. S. Hu, M. M. Titirici, *Carbon Energy.* **2022**, *4*, 914.
[44] a) Y. Zeng, J. Yang, H. Yang, Y. Yang, J. Zhao, *ACS Energy Lett.* **2024**, *9*, 1184; b) Z. H. Wang, X. Feng, Y. Bai, H. Y. Yang, R. Q. Dong, X. R. Wang, H. J. Xu, Q. Y. Wang, H. Li, H. C. Gao, C. Wu, *Adv. Energy Mater.* **2021**, *11*, 2003854.
[45] X. W. Dou, I. Hasa, D. Saurel, C. Vaalma, L. M. Wu, D. Buchholz, D. Bresser, S. Komaba, S. Passerini, *Mater. Today.* **2019**, *23*, 87.
[46] D. Cheng, X. Zhou, H. Hu, Z. Li, J. Chen, L. Miao, X. Ye, H. Zhang, *Carbon.* **2021**, *182*, 758.
[47] R. Q. Dong, L. M. Zheng, Y. Bai, Q. Ni, Y. Li, F. Wu, H. X. Ren, C. Wu, *Adv. Mater.* **2021**, *33*, 2008810.